Research Square

Preprints are preliminary reports that have not undergone peer review.
They should not be considered conclusive, used to inform clinical practice,
or referenced by the media as validated information.

Effect of micro rolling on laser-induced arc additive manufacturing of 2319 aluminum alloy

Zhaodong Zhang
Dalian University of Technology
Peisheng Li
Dalian University of Technology
Zijing Zhou
Dalian University of Technology
Gang Song
Dalian University of Technology
Xu Wang
wangxu@hqu.edu.cn

Huaqiao University

Research Article

Keywords: Additive manufacturing, Aluminum alloy, Laser induced arc, Rolling

Posted Date: September 8th, 2026

DOI: https://doi.org/10.21203/rs.3.rs-10610649/v1

License: This work is licensed under a Creative Commons Attribution 4.0 International License.
Read Full License

Effect of micro rolling on laser-induced arc additive manufacturing of 2319 aluminum alloy

Zhaodong Zhang[1], Peisheng Li[1], Zijing Zhou[1], Gang Song[1],

Xu Wang[2*]

[1]School of Material Science and Engineering, Dalian University of Technology, Key Laboratory of Liaoning Advanced Welding and Joining Technology, Dalian, China

[2]School of Material Science and Engineering, Huaqiao University, Xiamen, China

skyezzd@dlut.edu.cn;

lipeisheng2020@163.com;

zhouzijing@mail.dlut.edu.cn;

songgang@dlut.edu.cn;

* Corresponding: wangxu@hqu.edu.cn

Abstract

Laser-induced arc additive manufacturing (LIAAM) relies on arc energy with laser auxiliary regulation, effectively optimizing the forming quality and mechanical performance of conventional arc additive manufacturing. It possesses prominent advantages of high stacking rate, high material utilization, low cost, and the ability to manufacture large components. This paper introduces a novel LIAAM-rolling composite process to fabricate 2319 aluminum alloy and verify its effectiveness in forming quality and mechanical performance improvement. The results indicate that the LIAAM-rolling composite process significantly refines the microstructure. Rolled samples exhibit dispersed fine equiaxed grains and narrowed columnar crystal zones, with eutectic structures transforming from adverse reticulated morphology of the unrolled specimens to uniform dotted and rod-like structures. X-ray diffraction showed that the grain weave strength of the specimens fabricated by the laser-arc additive-rolling composite process was weakened and the anisotropy of the specimens was reduced. Compared with pure LIAAM samples, the rolled specimens achieve a 4.6% improvement in average hardness and a 9.13% enhancement in tensile strength, demonstrating great potential for high-performance aluminum alloy forming.

Keywords: Additive manufacturing; Aluminum alloy; Laser induced arc; Rolling

1 Introduction

In the context of global energy conservation and emission reduction, lightweight has become an unavoidable issue in the development of manufacturing industry. Aluminum metal is less dense, about 1/3 of iron, with good thermal conductivity, good corrosion resistance and easy to process and shape. Aluminum alloy has a wide range of applications in industrial manufacturing because of its low density, high strength, good forming performance, low relative cost and strong corrosion resistance[1]. Among them, 2-series aluminum alloys, as typical lightweight structural materials, occupy an important position in key fields such as

aerospace and national defense and military industry due to their excellent mechanical properties and good processing adaptability[2]. 2219 aluminum alloy is a representative 2-series aluminum alloy, in which copper serves as the core alloying element and achieves a remarkable solid-solution strengthening effect by forming the Al2Cu strengthening phase. And Mn element can greatly improve heat resistance and also reduce the generation of welding cracks. Lesser elements such as Ti, Zr, V, etc. have the effect of refining grain, improving alloy plasticity and improving thermal stability. Therefore, 2219 aluminum alloy has the advantages of high specific strength and stiffness, good weldability, wide working temperature range, good corrosion resistance and high fracture toughness.

As a high performance light alloy, aluminum alloy can be manufactured as a whole and complex aluminum alloy parts by using additive technology[3–5]. Aluminum alloy additive is mainly based on laser additive manufacturing (LAM) and wire arc additive manufacturing (WAAM). The more maturely developed processes for LAM are electron beam selective melting (EBSM) and selective laser melting (SLM). The high content of Cu elements in 2219-Al and the wide solidification temperature range make SLM forming process easy to produce defects such as porosity and thermal cracking, which seriously affect the comprehensive performance of the components.Solidification cracks are the main defects in the SLM additive manufacturing process of Al-Cu system alloys. Solidification cracks are formed during the solidification of the molten pool, mainly due to the stress accumulation value inside the component is higher than the bonding strength between the adjacent grains of the semi-solid metal, resulting in the grains being separated and cracks appearing[6]. In addition, the high thermal conductivity of aluminum alloy powder and the low absorption rate of laser also pose great difficulties for SLM forming aluminum alloy[7]. WAAM is becoming a promising additive manufacturing method due to the use of electric arc as the heat source and filler wire as the raw material, and the inherent advantages of high stacking rate, high material utilization, low cost and suitability for manufacturing large components. Therefore, WAAM of aluminum alloy has attracted a large number of scholars to study it.

In the field of aluminum alloy wire arc additive manufacturing (WAAM), there are conducted extensive research on process optimization and defect control. For example, Williams Stewart et al. [8, 9]systematically evaluated the mechanism of the effects of

parameters such as wire quality, droplet transfer, and inter - layer rolling on porosity and mechanical properties in the cold metal transfer (CMT) process. Gu et al. [10]and Kobayashi et al.[11] respectively confirmed the effect of the CMT process in refining grains and reducing porosity, as well as the harm of porosity defects in the Tungsten Inert Gas Welding (TIG) process to the mechanical properties of 2319/4043 aluminum alloys. The improved research by Wu et al. [5]and Ren et al. [12]showed that reducing the inter - layer temperature and introducing the hot - wire technology are effective ways to weaken anisotropy and improve deposition efficiency, respectively. However, single - arc additive manufacturing technology often suffers from poor forming quality and many defects, while laser additive manufacturing is limited by high costs. For this reason, Steen [13] proposed the laser - arc hybrid manufacturing technology in 1979. Faraji et al.[14] found that welding Al-Cu-Li alloy using a high laser power-low welding current strategy reduced the heat affect zone and improved the depth of melt. Sun et al.[15] prepared thin-walled aluminum alloy parts using a low-power laser-MIG based composite additive technique and found that the addition of laser could refine the structure and reduce the porosity content. However, it should be noted that while maintaining a relatively high deposition rate, it will introduce a large amount of heat accumulation. Severe deformation and residual stresses, as well as large grain sizes, may be generated during the fabrication process. The above problems will adversely affect the mechanical properties and fatigue behavior of the alloy.

In response to the above-mentioned challenges of tissue and performance degradation induced by heat accumulation, introducing interlayer rolling auxiliary technology is regarded as an effective means of collaborative regulation. Interlayer rolling assisted AM is a process where a roller rolls over the deposits Rolling is a method of improving the local mechanical properties of the processed material by moving the rolls to apply load. Li et al.[16] applied the rolling technique to the arc-enhanced process and found that the reduction in grain size due to rolling was due to grain recrystallization in the formed layer, which in turn was the result of micro-rolling in the subsequent layers. Colegrove et al.[17] used "shaped" or "slotted" rollers to roll each layer on the WAAM assembly. Compared to "shaped" rolls, "slotted" rolls are more effective in limiting transverse deformation and reducing longitudinal residual stress peaks. The interlayer rolling reheats the molten metal to refine its grain size. Interlayer rolling reheats

the molten metal and refines its grain size. Martina et al.[18] studied a Ti-6Al-4V alloy and found that rolling leads to a reduction in the overall thickness of the α photo layer, an early and significant refinement of the β-phase grains, and the formation of more equiaxed grains. This is due to the need for heat treatment during the deposition of the subsequent layers, which inevitably leads to recrystallization of the formed layers. Gu et al.[19] found that the interlayer rolling process can induce plastic deformation of the deposited metal and ultimately improve the mechanical properties of WAAM alloys in the form of higher density dislocations and lower orientation difference grains. Therefore, the wire arc additive manufacturing-rolling (WAAM-R) composite process can significantly improve the forming quality of the additive specimens at both macroscopic and microscopic levels, such as reducing macroscopic deformation and refining grains, thus improving the mechanical properties.

In this study, a new laser-induced arc additive manufacturing-rolling (LIAAM-R) composite process was developed to investigate the feasibility of using additive manufacturing technology to prepare 2319 aluminum alloy and improve the forming quality and mechanical properties. The microstructure evolution of the alloy was investigated in terms of grain morphology, element distribution and phase composition using a multi-scale characterization method. The change of grain morphology after rolling and the mechanism of cold deformation effects were studied. Finally, the relationship between the microstructure and mechanical properties of the deposited specimens was systematically established.

2 Materials and Methods

ER2319 aluminum wires with a diameter of 1.2 mm were used as feedstock and 2219-Al substrate with thickness of 5 mm utilized in this study. The chemical compositions are listed in Table 1. The AM system consists of an OTC FD-V20 robot, a WB-P500L welder and an LWS-800FK pulse laser. The composite heat source used in this study was composed of MIG arc and low power pulsed laser. The angle between the MIG torch and the substrate is 70°，the angle between the laser and the torch is 45°, which is for the low power laser induced arc additive manufacturing process. Before deposition, we need to remove impurities on the

substrate surface with a wire brush, and then clean the substrate surface with acetone. The YMH-1T welding mobile press was used to roll the deposited layer, and the specific experimental procedure is shown in Fig. 1. The shielding gas used for this experiment was argon with a purity of 99.99%. Table 2 lists the detailed arc, laser and rolling parameters used in the LIAAM experiment and in the experiments with the micro-rolling process, where the wire feed speed was automatically matched to the welding current.

Table 1. Chemical composition of wire and substrate (wt%)

Element	Cu	Si	Mn	Fe	Zr	V	Ti	Zn
ER2319	5.8-6.8	0.04	0.2-0.4	0.3	0.1-0.25	0.07	0.1-0.2	≤0.1

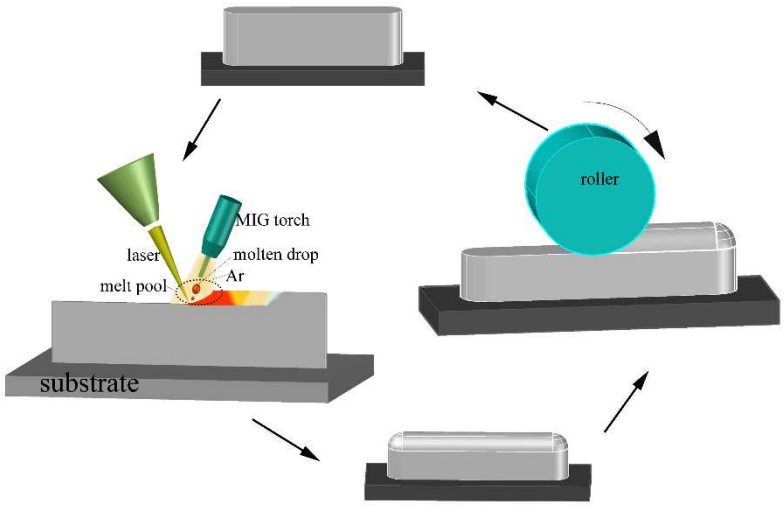


Fig. 1. Schematic diagram of the laser arc additive-rolling process.

Table 2. Experiment parameters.

Parameter	**LIAAM**	**LIAAM-R**
Average laser power (W)	320	320
Welding current (A)	120	120
Welding speed (mm/min)	450	450
Argon velocity (L/min)	20	20
Rolling height (mm)	-	1.5

Firstly, single pass multilayer additive manufacturing was performed using the LIAAM

process by adding a low power pulsed laser to a single MIG additive. The height of each layer was measured and 1.5 mm was selected as the height of each rolled layer based on the height difference between the maximum and minimum height of the same weld stripe, and single-pass multilayer additive manufacturing was performed using the LIAAM-R process. While improving the efficiency of the additive and increasing the material utilization, it is dedicated to increasing the stability of the deposition process and improving the forming quality and accuracy of the structural parts. Then we compare the surface forming quality and mechanical properties of the four groups of specimens, observe the tissue characteristics of LIAAM and LIAAM-R samples using metallurgical microscopy and scanning electron microscopy, observe the fracture morphology and analyze the fracture mechanism. Finally, we analyze the mechanism of cold deformation in the process of laser-induced arc additive, analyze the tissue changes, physical phase composition, and finally explore the reasons for the performance improvement.

The specimens obtained under both processes were sampled as shown in Fig. 2. Four tensile samples were taken from each specimen for measuring tensile properties, and one metallographic sample was taken in the middle for microstructure observation and physical phase analysis. Metallographic samples were polished and polished in an anodic coating solution (HBF_4: H_2O = 1: 40) at a constant voltage of 20 V for 150 s. The cross-sectional weld fusion macroscopic morphology was directly visible, and the microstructure of the specimen was observed using a Zeiss HAL-100 polarized light microscope. The hardness was measured at 0.25 mm intervals in the center of the cross-section, starting from the bottom of the first fusion line, to obtain the hardness profile of the specimen surface, loaded with 200 gf and

holding time of 10 s. The deposited specimens were observed by SEM for microscopic and fracture morphology and energy spectrum analysis. In addition, X-ray diffraction was performed using CuKα radiation at a scanning step interval of 0.04° in the 2θ range of 20°-100° to obtain the data.

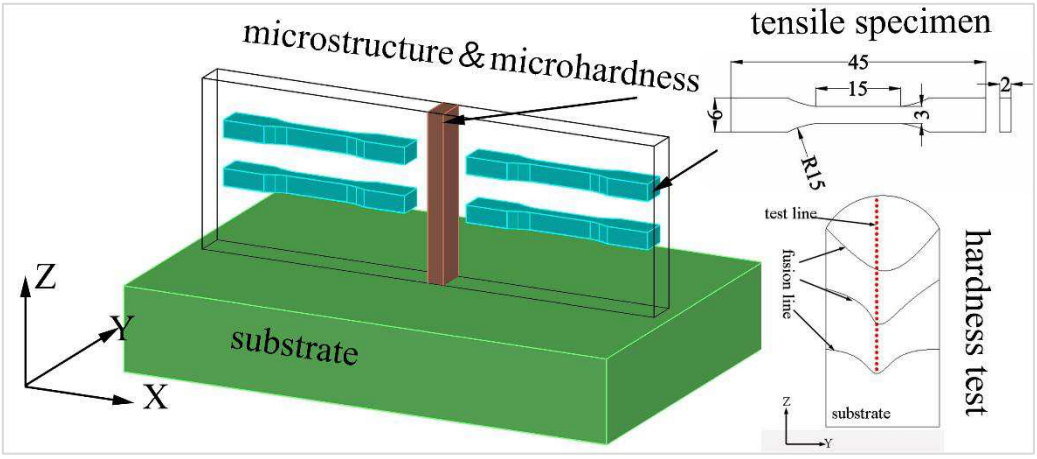


Fig. 2. Sampling method.

3 Results

3.1 Macrostructures

Fig. 3 shows the macroscopic morphology and cross-section of LIAAM and LIAAM-R samples. The dotted lines are the bond with the base material and the interlayer bond, H is the total height of the specimen, and L is the width of the specimen. From Fig. 3, it can be seen that the surface of the specimen is relatively flat after rolling, with pits at the extinguished end. With reciprocal additions, the depressions caused by arc extinguishing are smaller and filled by the next cladding layer, and only the last cladding layer will show smaller depressions. The cross-sectional view shows good layer-to-layer metallurgy with no obvious cracks or defects under both processes.

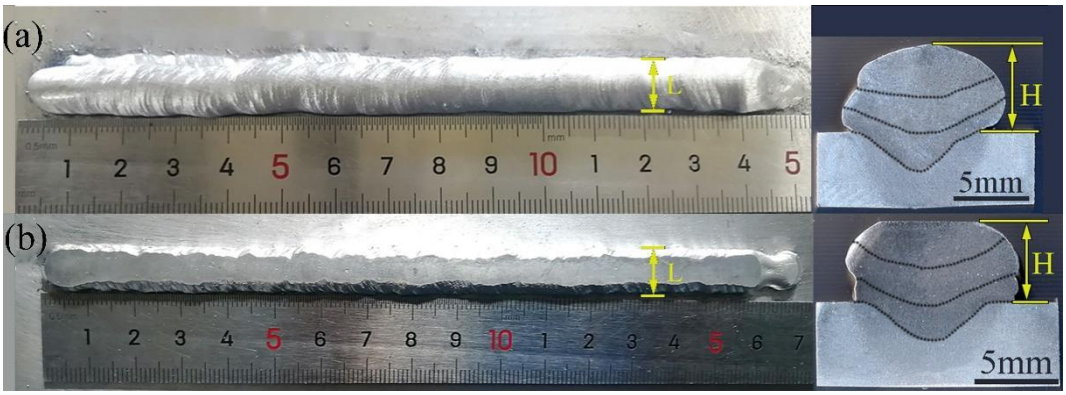


Fig. 3. Macro topography and cross-sectional image of parts. (a) LIAAM; (b) LIAAM-R.

Table 3 shows the geometry and deformation parameters of LIAAM and LIAAM-R specimens, where △h is the average height between the dashed lines in Fig. 3, △L is the average width of each layer, δH is the total height deformation, δ△h is the average height deformation, and δ△L is the average width deformation. The height of the three-layer single-pass specimen under LIAAM process is 6.3 mm, while the height of the three-layer single-pass specimen under LIAAM-R of three-layer single-lane specimen height is 5.2 mm, compared with the former deformation rate of about 17.46%, compared with the single-layer single-lane specimen deformation rate of 15.73% increased by 1.73%, a slight increase in deformation rate, but observation of the first two layers of the deposition layer height under the two process states can be found, the height of one layer of deposition layer LIAAM is 2.7 mm, LIAAM-R is 1.88 mm, and In the additive manufacturing process, the height difference between rolled and unrolled specimens changed less with each layer change, and the height of rolled specimens did not decrease significantly with the accumulation of rolling times. The reasons for this phenomenon are: first, because LIAAM is less stable and there is a certain error in the layer height of each deposited stripe in the deposition process; second, because the incremental manufacturing is a layer-by-layer incremental manufacturing process, and the latter layer produces a remelting effect on the previous deposited layer when deposited, which leads to the deformation produced by rolling on the previous layer almost disappears, and the incremental

manufacturing does not continue after the third layer is rolled, so the LIAAM-R The total height of the specimen was lower. After rolling, the ripples formed due to arc instability were flattened by the rolls and the surface quality of each molten layer was improved, providing better conditions for the next layer to be molten.

Table 3. Parameters of geometry and distortion.

Processing	Number of layers	H/mm	$_{\Delta}$h/mm	$_{\Delta}$L/mm	δ_H/%	$\delta_{\Delta h}$/%	$\delta_{\Delta L}$/%
LIAAM	3	6.3	2.67	9.2	17.46	15.73	14.13
LIAAM-R	3	5.2	2.25	10.5			

3.2 Grain morphology and pores

Figs. 4 and 5 show the different observation positions and microstructures of LIAAM specimens and LIAAM-R specimens, respectively. Figs. 4(a) and 5(a) show cross-sectional views with three red boxes indicating the regions examined by optical microscopy from bottom to top. At the bottom of both specimens (Figs. 4(d) and 5(d)), dendrites dominate, along with some defects, dendrite fragmentation, and grain-boundary coarsening. In the middle region of the LIAAM specimen (Fig. 4(c)), the columnar crystal zone is narrower, mainly dominated by larger equiaxed crystals and columnar dendrites, and the columnar dendrites also have a more consistent growth trend, after interlayer rolling The middle part (Fig. 5(c)) has fine equiaxed crystals in the lower region, and columnar crystals and dendrites in the upper region, respectively, while fine equiaxed crystals are uniformly distributed between the grains, and the columnar crystals have a consistent growth trend with obvious anisotropy. At the top of both specimens (Figs. 4(b) and 5(b)), dendrites are prevalent, with a dense dendritic structure. The LIAAM-R specimen exhibits smaller grains and a higher number of grains in the direction perpendicular to the rolling force compared with the LIAAM specimen.

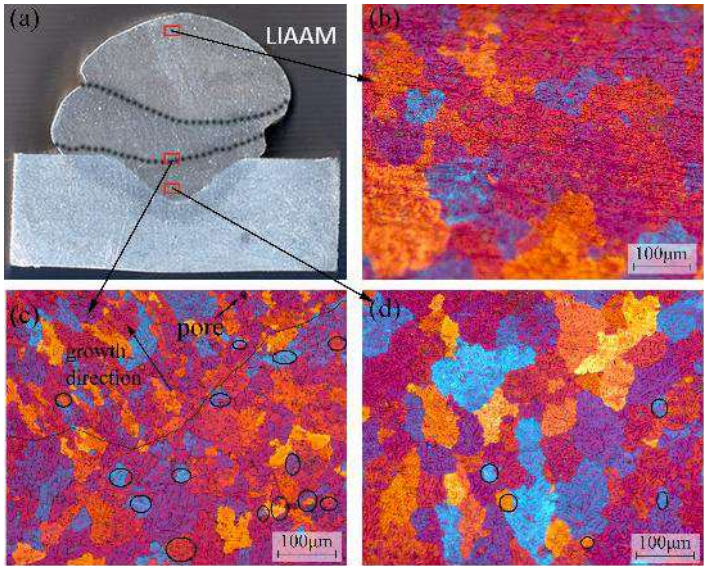


Fig. 4. Different observation positions and microstructures of LIAAM specimen. (a) Optical microscope observation position; (b) top microstructure; (c) middle microstructure; (d) bottom microstructure.

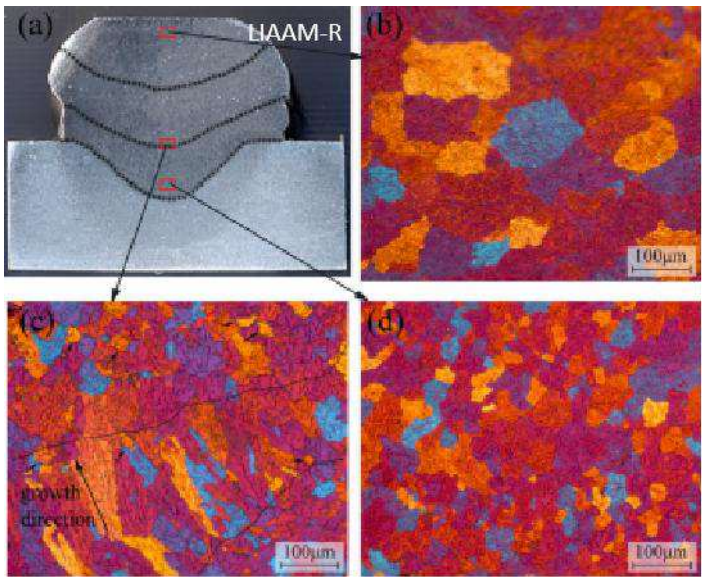


Fig. 5. Different observation positions and microstructures of LIAAM-R specimen. (a) Optical microscope observation position; (b) top microstructure; (c) middle microstructure; (d) bottom microstructure.

Smaller equiaxed crystals appear under the action of laser stirring. The central equiaxial crystal zone is larger in both sets of specimens, and Fig. 6 shows the distribution of equiaxial crystals in the middle of the specimens. Fig. 6(a) shows the central equiaxial crystal zone of the LIAAM specimen, and the average grain size of the equiaxial crystals is 38.77 μm. The smaller equiaxial crystals are marked by circles in the Fig. 6, and they are diffusely distributed

throughout the equiaxial crystal zone. Fig. 6(b) shows the central equiaxial crystal zone of the LIAAM-R specimen, and it can be seen that the equiaxial crystals in the upper half are significantly smaller, and the size of the equiaxial crystals in the lower half is not uniform. Since the surface of laser-induced arc accretion is smoother than the surface of arc accretion and the downward pressure height is smaller, no continuous isometric crystal zone is formed in the middle of the specimen, and only diffusely distributed isometric crystals are present. Therefore, LIAAM-R specimens have finer grains, more equiaxed crystals and narrower columnar crystal zones than LIAAM specimens. The larger equiaxed crystals are influenced by heat accumulation and grain growth.

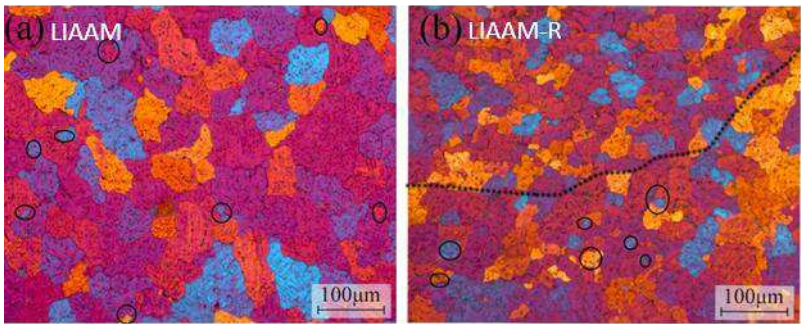


Fig. 6. Equiaxed grain of specimens. (a) LIAAM; (b) LIAAM-R.

A large number of slip and twin bands appear inside the grain under pressure, while the grain will gradually elongate in the direction of its deformation. Isometric, dendritic, columnar and columnar dendritic crystals will appear in the incremental specimens. With increasing pressure, the grains are elongated, and the dendrites and columnar dendrites are difficult to observe after rolling because of the many developed dendrites. Theoretically, columnar crystals can achieve the effect of eliminating anisotropy with the increase of deformation, but equiaxed crystals become elongated and fibrous with obvious anisotropy. Since small pressure rolling is used during the enlargement process and the top area of the LIAAM specimen is almost dendritic, there is no elongation of the equiaxed crystals.

Porosity is detrimental to the fatigue, strength and toughness of aluminum alloys, and

porosity can lead to strain concentrations that can create load carrying capacity and lead to premature fracture[20]. Studies have shown that the pore size of aluminum alloy specimens is reduced under the agitation of laser[21]. The pore size distribution of LIAAM specimens and LIAAM-R specimens is shown in Fig. 7. The pore diameters of LIAAM-R specimens were mainly in the range of 10-40 μm, with the most pores in the range of 20-40 μm, with an average diameter of 32.21 μm, a maximum diameter of 72.61 μm and a minimum diameter of 14.08 μm. The number of pores decreased significantly after rolling, and the average diameter of pores decreased.

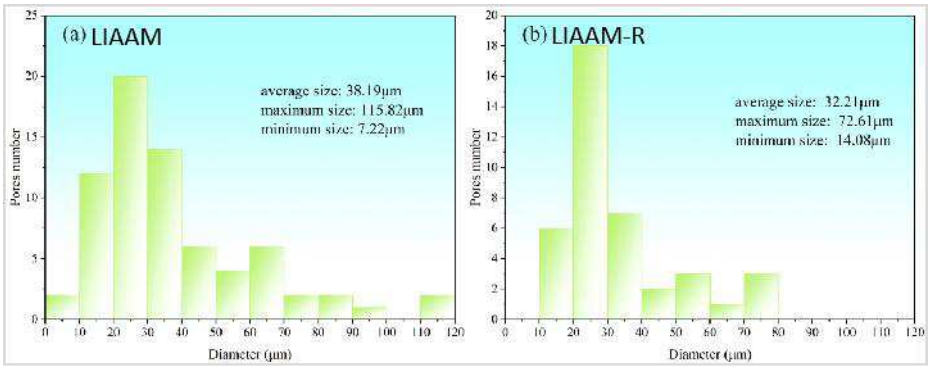


Fig. 7. Pores size distribution diagram. (a) LIAAM; (b) LIAAM-R.

3.3 Second phase and eutectic tissue distribution

ER2319-Al wire takes α-Al as the matrix and can dissolve a certain amount of Cu elements to become α-Al solid solution. Among them, the θ-Al_2Cu phase can be precipitated simultaneously with α-Al during the solidification of liquid aluminum alloy, which constitutes the eutectic organization of the material, and the eutectic organization is a lamellar structure with large volume, which can be observed under scanning electron microscopy[22]. While the θ'-Al_2Cu phase and θ''-Al_2Cu phase mainly precipitate from solid α-Al. Since the θ''-Al_2Cu phase and θ'-Al_2Cu phase are transition phases, they have a semi-eutectic structure with the α-Al matrix and can play a significant precipitation strengthening effect. The θ''-Al_2Cu and θ'-Al_2Cu phases will be transformed into equilibrium θ-Al_2Cu phases after aging, and the precipitation strengthening effect will gradually disappear.

Fig. 8 shows the XRD results of the LIAAM and LIAAM-R samples, and it can be seen that the diffraction peaks of α-Al and Al_2Cu are observed for both groups of samples. Also the intensity of the (111) Bragg peak is significantly enhanced and the intensity of the (200) Bragg peak is reduced in the LIAAM-R sample compared to the LIAAM sample. The intensity ratio of the Al (111) peak to the Al (200) peak can serve as an indicator for evaluating weave texture. It reveals that the texture strength of the LIAAM-R sample is reduced.

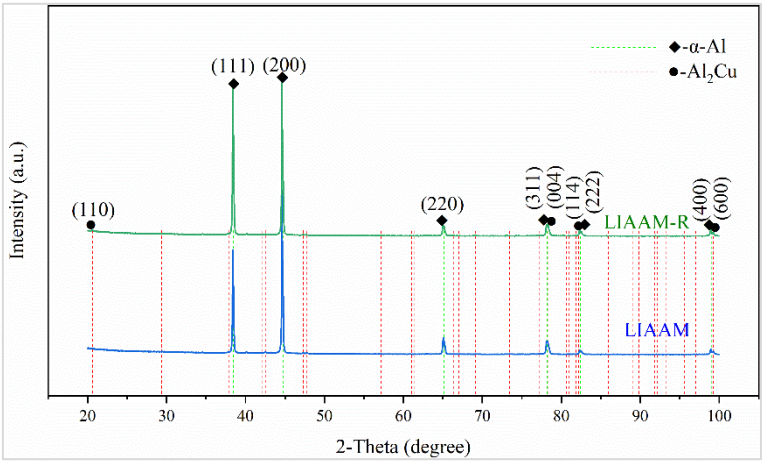


Fig. 8. XRD spectrums of 2319 Al alloy LIAAM and LIAAM-R specimens.

Fig. 9 shows the SEM image, where a large amount of white tissue can be found distributed on the black matrix. These white tissues are morphologically dominated by dots and short rods, mainly distributed at grain boundaries or subgrain boundaries. The dashed line shows the demarcation line of the interlayer tissue, and it can be seen that the lower layer of the LIAAM specimen has reticulated white tissue, while the lower layer of the LIAAM-R specimen is dominated by short rod-like tissue. The results of the energy spectrum test in Fig. 10 show that the content of Cu elements in the white tissue is 31.37% and the mass ratio of eutectic tissue close to the Al-Cu alloy is 67/33[6]. It can be judged as a eutectic organization (α-Al + θ-Al_2Cu) precipitated in the liquid phase. And the content of Cu in the black matrix is 2.43%, which can be judged as an α-Al matrix with dissolved Cu elements, i.e. α-Al solid solution. The reticular eutectic organization is due to the continuous thermal accumulation and

the continuous development from point-like[23], which can generate defects and tissue coarsening during the growth process and affect the properties.

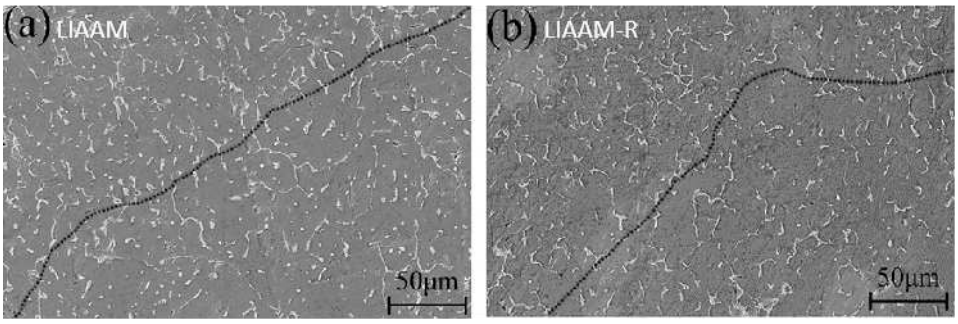


Fig. 9. Eutectics in interlayer transition region of 2319-Al deposited specimen. (a) LIAAM; (b) LIAAM-R.

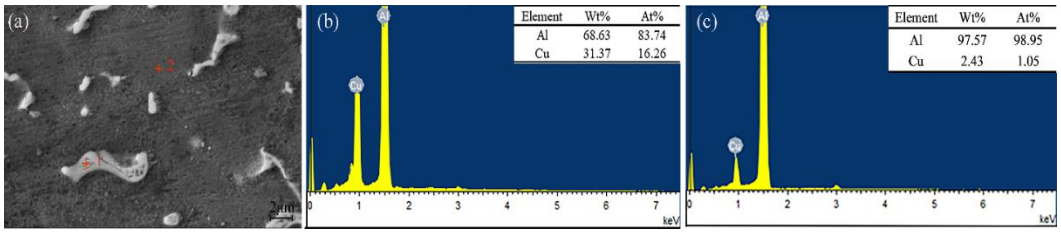


Fig. 10. EDS results for 2319-Al deposited specimen. (a) morphology of second phase; (b) EDS result at point 1; (c) EDS result at point 2.

Figs. 11 and 12 show the results of electron probe micro-analysis (EPMA) in the interlayer region for LIAAM specimens and LIAAM-R specimens, respectively, where Figs. 11(a) and 12(a) are the backscattering map of the specimens, and Figs. 11(b-d) and 12(b-d) are the distribution maps of Al, Cu and Mn elements in the corresponding regions, respectively. It can be seen from the plots that the specimens are mainly composed of Al elements, Cu elements are mainly aggregated at grain boundaries or subgrain boundaries and present in the eutectic organization of grain boundaries, and Mn elements are less abundant. From the comparison of Figs. 11(c) and 12(c), it can be found that a large number of longer bar-like aggregates of Cu elements appear in the LIAAM specimens, while the Cu elements in the LIAAM-R specimens are mainly grain-like aggregates and short bar-like aggregates, which are consistent with the morphology of the eutectic organization. From the comparison of Figs. 11(d) and 12(d), it can be found that the LIAAM specimens have some Mn element aggregates, while the LIAAM-R specimens have a more uniform distribution of Mn elements. In terms of elemental distribution,

both Cu and Mn elements in the LIAAM-R specimens are more dispersed, and elemental segregation is reduced. This is due to the lower deposition layer and faster heat dissipation after rolling, i.e., the material melting and solidification rate is elevated, the temperature gradient increases, the cooling rate and solidification rate of the melt pool increases, and the solute diffusion is inhibited, so the element distribution is more uniform[24]. The grain size can affect the degree of segregation, and a comparison of the microstructure of the two groups of specimens shows that the LIAAM-R specimen has a smaller overall grain size and therefore a more uniform distribution of elements. Cu elements can form Al_2Cu, which plays the role of solid solution strengthening, and the diffuse distribution of Cu elements increases the precipitation phase and enhances the strengthening effect. The role of Mn elements in aluminum alloys is to reduce the generation of weld cracks, therefore, the reduction of Mn element segregation in LIAAM-R specimens can reduce the crack generation rate of the specimens.

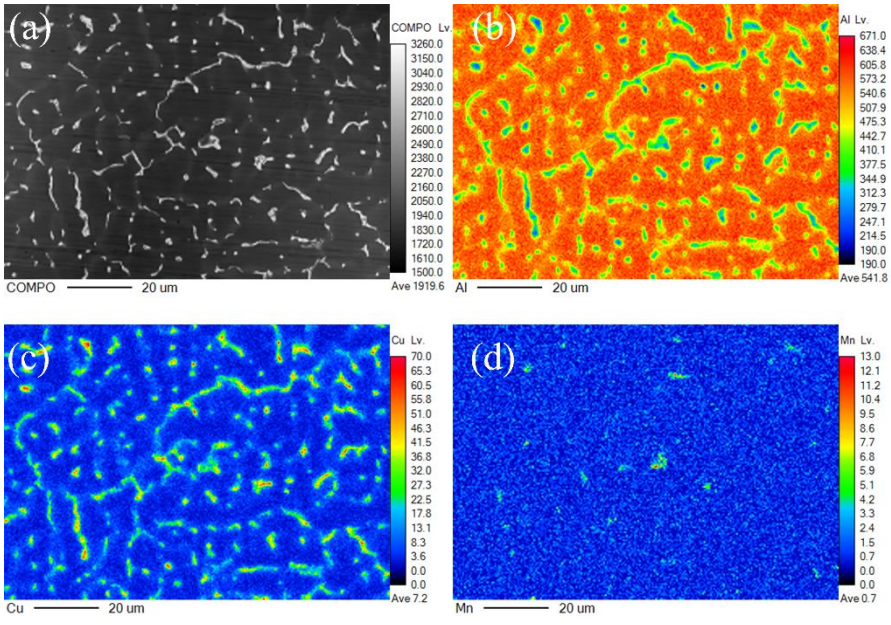


Fig. 11. EPMA results of the interlayer region in LIAAM specimen. (a) backscattering map; (b) Al element distribution; (c) Cu element distribution; (d) Mn element distribution.

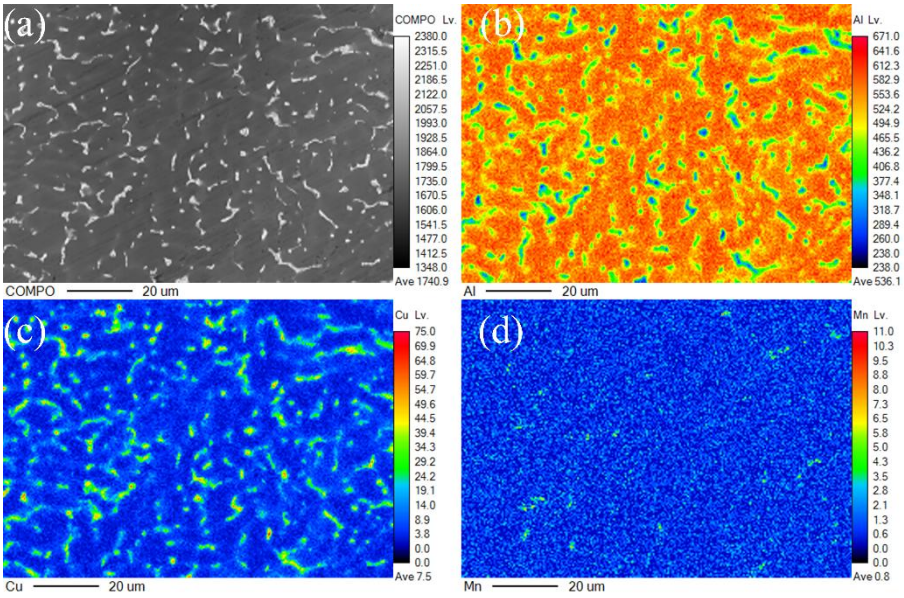


Fig. 12. EPMA results of the interlayer region in LIAAM-R specimen. (a) backscattering map; (b) Al element distribution; (c) Cu element distribution; (d) Mn element distribution.

3.4 Mechanical properties

Fig. 13 shows the hardness distribution of LIAAM and LIAAM-R specimens from the bottom to the top. the average hardness of LIAAM specimens and LIAAM-R specimens are 91.41HV0.2 and 95.61HV0.2, respectively. after rolling, the average hardness is increased by 4.6%. It can be seen from the graph that after rolling, the top hardness is higher than unrolled, and the other areas do not change much in hardness. This is due to the significant work hardening effect of the last layer. As a result of cold deformation in the lower and middle parts, the next melt layer is created so that the deformed grains recrystallize in return, eliminating the work-hardening effect. After rolling the hardness change is much less undulating and there is no point of sudden hardness drop, which indicates that after rolling the specimen has fewer defects and more uniform grains.

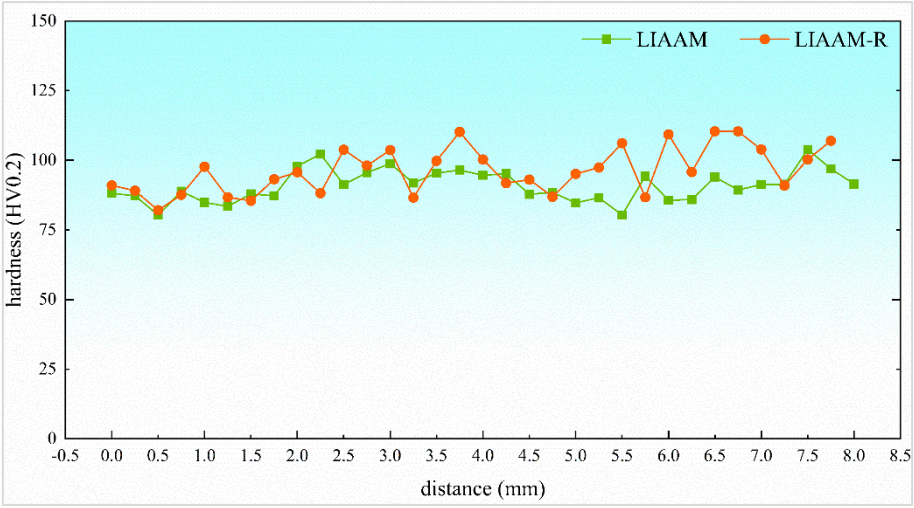


Fig. 13. Hardness distribution of LIAAM and LIAAM-R specimens.

Fig. 14 shows the tensile properties of the specimens under different processes. The tensile strengths of LIAAM and LIAAM-R were 262 MPa and 285.91 MPa, respectively, and the elongation was 17.99% and 11.18%, respectively, which increased by 9.13% after rolling and decreased by 37.85% after elongation. The specimens fabricated by the arc-amplification-rolling composite process showed an increase in tensile strength of 28.21% and an increase in elongation after break of 12.02%. Gu et al.[19] showed a 20% increase in tensile strength and a 40% decrease in post-extension at break using CMT additive + 45 KN rolling. Therefore, LIAAM-R process has a greater enhancement of specimen performance.

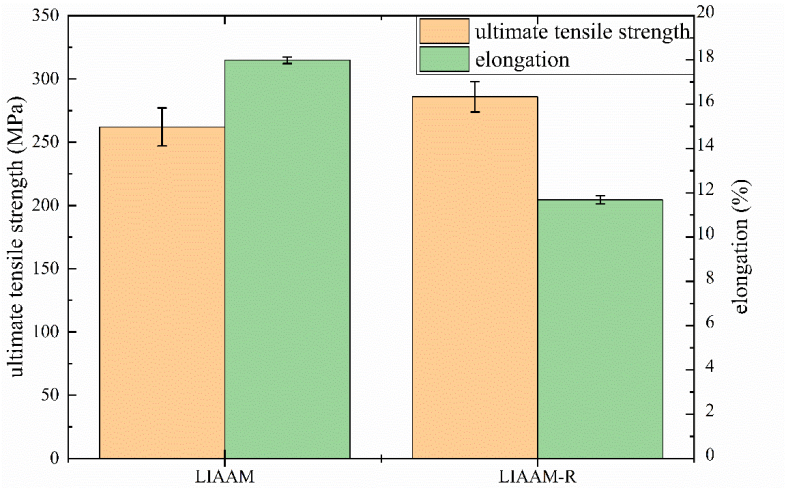


Fig. 14. Tensile property diagram.

3.5 Fracture morphology

Fig. 15 shows the fracture morphology of the two groups of specimens. Fig. 15(a) shows the macroscopic shape of the fracture of the LIAAM specimen, with more large pores gathered in the upper right part of the fracture and smaller pores in other areas. Fig. 15(c) is the macroscopic view of the fracture of LIAAM-R specimen, with smaller pores and uniform distribution. From Figs. 15(b,d), it can be seen that the dimples of LIAAM are larger, and there are granular and lamellar precipitates inside the dimples, and the dimples of LIAAM-R are finer and more uniform, and the precipitated phases inside the tough nests are granular. The energy spectrum analysis of the precipitated phases shows that both LIAAM and LIAAM-R fracture precipitated phases are composed of Al_2Cu. It was found that both LIAAM and LIAAM-R tensile specimens fractured by ductile fracture. However, the LIAAM-R specimens had fewer pores in the fracture, smaller and denser toughness nests, and no large pore aggregation. According to the comparison of the tensile properties of the two groups of specimens, it can be found that the size of the pores inside the specimens has a greater effect on the strength, and the size of the pores does not have an effect on the elongation. Also the morphology of the precipitates had an effect on the tensile properties of the specimens.

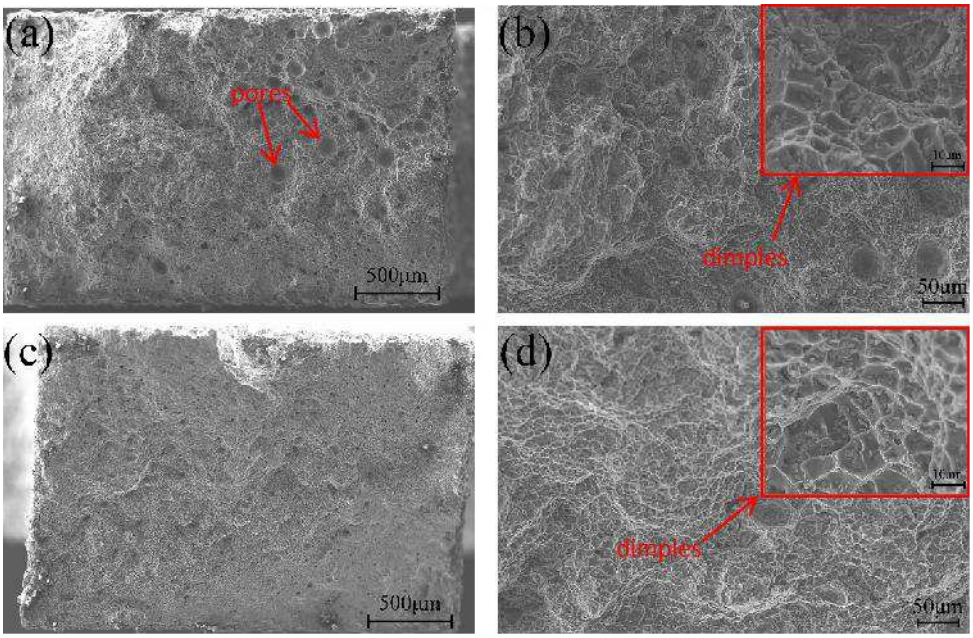


Fig. 15. Fracture morphology. (a) macroscopic morphology and (b) enlarged view of the tough fossa of LIAAM; (c) macroscopic morphology and (d) enlarged view of the tough fossa of LIAAM-R.

A large number of second-phase particles appear in the tough nest of the specimen, and the second-phase particles are the source of microporous forming. The diffuse reinforcement has a strengthening effect on the specimen, but under high strain conditions, a large number of dislocations appear, causing dislocation plugging, and the second phase is not coordinated with the plastic deformation of the body and sprouting microporosity. In addition, the crack tip and microporous, microporous and microporous local slip occurs between the microporous, will make the microporous more rapid aggregation, the plastic toughness of the material is worse. The plastic deformation formula is as follows, where α is the softness coefficient of the stress state, τ_{max} is the maximum tangential stress, and Smax is the maximum equivalent positive stress.

$$\alpha = \tau_{max}/S_{max} \quad (1)$$

According to Equation (1), the higher the positive stress, the smaller the α, and the more likely to form cracking, so the choice of small stress rolling in the rolling process can reduce the microporous aggregation and effectively avoid cracking. in the fracture of LIAAM-R specimen (Fig. 15(c)), it can be seen that the holes are more uniformly distributed, so the tensile strength is higher.

4 Discussion

4.1 Strengthening mechanism

The strengthening mechanism of the composite process of AM + rolling is specifically work-hardening and heat treatment strengthening. Small pressure rolling increases dislocations after cold deformation, which plays the effect of process hardening, and the next layer of fusion cladding plays the effect of heat treatment.

The surface of the specimen is changed from a curved shape with high middle and low ends to a flat surface, Fig. 16 is a schematic diagram of the change in cross-sectional

morphology before and after rolling. After the downward pressure applied by the roll, the specimen undergoes plastic deformation. The plastic deformation of crystals is by means of dislocations under stress, continuous movement and proliferation, so after plastic deformation, the dislocation density increases. The reinforcing effect of work-hardening can be expressed in Equation (2):

$$\tau=\tau_0+A\rho^{1/2} \quad (2)$$

where τ is the parting stress required to maintain plastic flow, τ_0 is the shear stress required for other factors to impede dislocation movement, A is an empirical constant, and ρ is the dislocation density. As the dislocation density increases, the deformation resistance of the material is enhanced. Based on the comparison of the properties of the two sets of specimens, the hardness and tensile strength of the specimens increase after cold deformation.

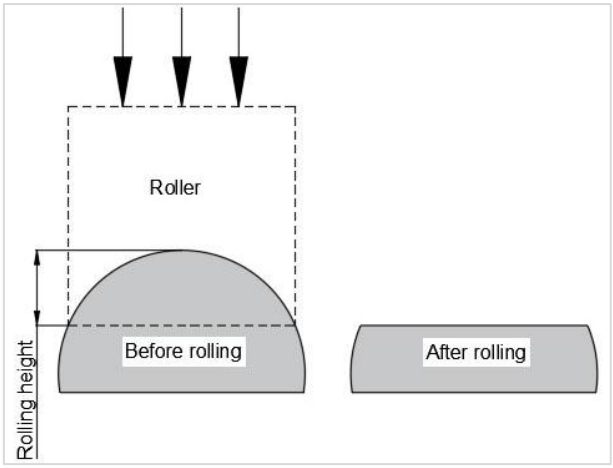


Fig. 16. Cross-sectional morphology before and after rolling.

The top of the LIAAM-R specimen was rolled without re-melting, and the overall microstructure of the specimen shows that the small pressure rolling did not produce the typical fiber tissue structure, which is due to the fact that the microstructure of the additive specimen has fewer equiaxed crystals, and the columnar and dendritic crystals are all growing toward the center of the melt pool, and the texture direction formed by the additive manufacturing process is perpendicular to the rolling force. The XRD results (Fig. 8) show that the texture strength of

the specimens became weaker after rolling. At the same time, after plastic deformation, the density of structural defects such as dislocation vacancies increases, as well as the distortion energy increases, which puts the specimen in a thermodynamically unstable and high free energy state. For the top of the specimen, after cold deformation, the dendritic spacing of the top dendrites becomes smaller. For the middle and lower part of the specimen, after cold deformation by complex thermal cycling, the dendrites of the upper layer change toward the deformation direction after rolling, and the area with large distortion degree produces a new grain core without distortion, and the next layer plays the effect of heat treatment when fusing, and grows by gradually consuming the surrounding deformed matrix on the grain core until a fine equiaxial crystal is formed, and the schematic diagram of the grain change in the middle and lower part of the LIAAM-R specimen , as shown in Fig. 17.

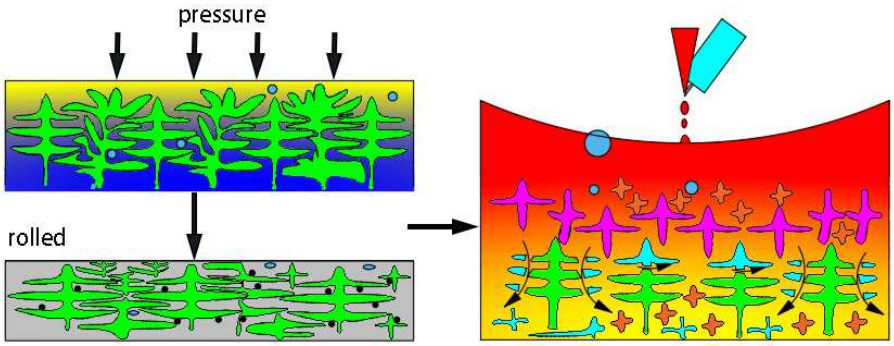


Fig. 17. Schematic diagram of grain variation in the middle and lower parts of LIAAM-R specimen.

Comparing from the microstructure, the grain size of LIAAM-R specimen becomes smaller and the addition of rolling process has a fine grain strengthening effect on the specimens, which can be expressed by Hall-Petch Equation (3):

$$\sigma_s = \sigma_0 + K d^{-1/2} \quad (3)$$

where σ_s is the yield strength of the polycrystal, d is the average diameter of the grain, σ_0 is the intracrystalline resistance to deformation, and K is the coefficient of influence of grain boundaries on deformation, which is related to the structure of the grain boundaries. The smaller the grain size, the higher the number of grains and the higher the number of grain

boundaries. Due to the severe dot distortion on the grain boundary and the different grain orientation on both sides of the grain boundary, the grain boundary impedes the dislocation slip between adjacent grains. Therefore, the finer the grains, the greater the applied stress required to produce macroscopic plastic deformation.

The pore morphology in aluminum alloy AM specimens is mainly spherical, and during the additive manufacturing process, the pores are mainly due to some air bubbles trapped in the molten pool during the melting process in the inert gas environment, forming spherical pores[25]. Due to the rolling force, the size of the pores becomes smaller or disappears, and after the middle and lower deposited layers are remelted, the pores grow and overflow into the melt pool by heated. The distribution of pores in the specimens (Fig. 7) also shows that the number of pores in LIAAM-R specimens decreases and the average size of pores decreases. The size, shape and spatial distribution of the defects significantly affect the fatigue properties of the metal, especially the location and size of the defects. If the defects are located close to the surface, the fatigue life of the sample will be much shorter than if the defects are located far from the surface[26]. From the fracture morphology, it can be seen that the LIAAM-R specimens have uniform distribution of pores and increased ultimate tensile strength.

In summary, from the viewpoint of microstructure, texture strength and defect distribution, rolling is favorable to the mechanical properties of the specimens, and the ultimate tensile strength and average hardness of LIAAM-R specimens are improved from the mechanical properties of LIAAM specimens and LIAAM-R specimens.

5 Conclusions

In this paper, a novel laser-induced arc additive manufacturing-rolling (LIAAM-R) composite process was adopted to fabricate 2319 aluminum alloy, and the differences in macroscopic forming quality, microstructure characteristics and mechanical properties between conventional pure LIAAM process and LIAAM-R composite process were

systematically investigated. The main conclusions were shown as follows:

(1) Macroscopically, the macroscopic surface of LIAAM-R specimens is flatter and more conducive to forming the next layer after each layer has been rolled. The 1.5 mm rolling reduction corresponds to a significant thickness strain of approximately 30%, indicating substantial plastic deformation.

(2) Microscopically, the eutectic structure of the LIAAM specimen has a reticular structure, which affects the properties. After rolling, diffuse fine equiaxed crystals appear in the middle of the specimen, the columnar crystal zone becomes narrower andthe eutectic structure of the specimen disappeared, the texture strength of the grains became weaker, the anisotropy of the specimen as a whole was reduced, and the distribution of Cu and Mn elements was more uniform.

(3) Mechanically, the LIAAM-R specimen exhibits a 4.6% increase in average hardness and a 9.13% increase in tensile strength in comparison with the LIAAM specimen, which are attributed to the synergistic effects of work hardening, grain refinement, and precipitation strengthening.

(4) Fractographically, the LIAAM specimen shows pore aggregation in the fracture, which promotes crack initiation, where lamellar precipitates are detrimental to performance. The LIAAM-R specimen exhibits more uniform pore distribution, which benefit to mechanical improvement.

Author contribution

Zhaodong Zhang: conceptualization, methodology, data curation, formal analysis, writing — original draft. Peisheng Li: data curation, formal analysis, investigation. Xu Wang: conceptualization, methodology, funding acquisition, supervision, writing — review and editing. Zijing Zhou: investigation, validation, visualization. Gang Song: supervision, resources, writing — review and editing.

Funding

This work was supported by the Joint Funds of the National Natural Science Foundation of China (U1960111) and the Fundamental Research Funds for the Central Universities (DUTZD25106).

Data Availability

The original contributions presented in this study are included in the article. Further inquiries can be directed to the corresponding author.

Declarations

Competing interests The authors declare no competing interests.

References

1. Srivatsav S, Jayakumar V, Sathishkumar M (2021) Recent developments and challenges associated with wire arc additive manufacturing of Al alloy: A review. Mater Today Proc 46:8561–8566. https://doi.org/10.1016/j.matpr.2021.03.542

2. Li R, Zhang H, Dai F, et al (2019) End lateral extension path strategy for intersection in wire and arc additive manufactured 2319 aluminum alloy. Rapid Prototyp J 26:360–369. https://doi.org/10.1108/RPJ-05-2019-0123

3. Buchanan C, Gardner L (2019) Metal 3D printing in construction: A review of methods, research, applications, opportunities and challenges. Eng Struct 180:332–348. https://doi.org/10.1016/j.engstruct.2018.11.045

4. Williams SW, Martina F, Addison AC, et al (2016) Wire + Arc Additive Manufacturing. Mater Sci Technol 32:641–647. https://doi.org/10.1179/1743284715Y.0000000073

5. Wu B, Pan Z, Ding D, et al (2018) Effects of heat accumulation on microstructure and mechanical properties of Ti6Al4V alloy deposited by wire arc additive manufacturing. Addit Manuf 23:151–160. https://doi.org/10.1016/j.addma.2018.08.004

6. Li Z, Ou L, Wang Y, et al (2023) Solidification Cracking Restraining Mechanism of Al-Cu-Mg-Zn Alloy Welds Using Cold Metal Transfer Technique. Materials 16:721. https://doi.org/10.3390/ma16020721

7. Liu M, Ma G, Liu D, et al (2020) Microstructure and mechanical properties of aluminum alloy prepared by laser-arc hybrid additive manufacturing. J Laser Appl 32:022052. https://doi.org/10.2351/7.0000082

8. Cong B, Ding J, Williams S (2015) Effect of arc mode in cold metal transfer process on porosity of additively manufactured Al-6.3%Cu alloy. Int J Adv Manuf Technol 76:1593–1606. https://doi.org/10.1007/s00170-014-6346-x

9. Hönnige JR, Colegrove PA, Ganguly S, et al (2018) Control of residual stress and distortion in aluminium wire + arc additive manufacture with rolling. Addit Manuf 22:775–783. https://doi.org/10.1016/j.addma.2018.06.015

10. Gu J, Ding J, Williams SW, et al (2016) The strengthening effect of inter-layer cold working and post-deposition heat treatment on the additively manufactured Al–6.3Cu alloy. Mater Sci Eng A 651:18–26. https://doi.org/10.1016/j.msea.2015.10.101

11. Kobayashi M, Dorce Y, Toda H, Horikawa H (2010) Effect of local volume fraction of microporosity on tensile properties in Al–Si–Mg cast alloy. Mater Sci Technol 26:962–967. https://doi.org/10.1179/174328409X441283

12. Ren L, Gu H, Wang W, et al (2019) Effects of Interpass Cooling on Material Properties of Wire Arc Additive Manufactured Al–6.3Mg Alloy. 3D Print Addit Manuf 6:344–353. https://doi.org/10.1089/3dp.2019.0061

13. Steen WM (1980) Arc augmented laser processing of materials. J Appl Phys 51:5636–5641. https://doi.org/10.1063/1.327560

14. Faraji AH, Moradi M, Goodarzi M, et al (2017) An investigation on capability of hybrid Nd:YAG laser-TIG welding technology for AA2198 Al-Li alloy. Opt Lasers Eng 96:1–6. https://doi.org/10.1016/j.optlaseng.2017.04.004

15. Zhang Z, Sun C, Xu X, Liu L (2018) Surface quality and forming characteristics of thin-wall aluminium alloy parts manufactured by laser assisted MIG arc additive manufacturing. Int J Lightweight Mater Manuf 1:89–95. https://doi.org/10.1016/j.ijlmm.2018.03.005

16. Li F, Shi W, Bian N, Wu H-B (2015) Effect of Accumulative Strain on Grain Refinement and Strengthening of ZM6 Magnesium Alloy During Continuous Variable Cross-Section Direct Extrusion. Acta Metall Sin Engl Lett 28:649–655. https://doi.org/10.1007/s40195-015-0245-5

17. Colegrove PA, Coules HE, Fairman J, et al (2013) Microstructure and residual stress improvement in wire and arc additively manufactured parts through high-pressure rolling. J Mater Process Technol 213:1782–1791. https://doi.org/10.1016/j.jmatprotec.2013.04.012

18. Martina F, Colegrove PA, Williams SW, Meyer J (2015) Microstructure of Interpass Rolled Wire + Arc Additive Manufacturing Ti-6Al-4V Components. Metall Mater Trans A 46:6103–6118. https://doi.org/10.1007/s11661-015-3172-1

19. Gu J, Bai J, Ding J, et al (2018) Design and cracking susceptibility of additively manufactured Al-Cu-Mg alloys with tandem wires and pulsed arc. J Mater Process Technol 262:210–220. https://doi.org/10.1016/j.jmatprotec.2018.06.030

20. Gu J, Yang S, Gao M, et al (2020) Micropore evolution in additively manufactured aluminum alloys under heat treatment and inter-layer rolling. Mater Des 186:108288. https://doi.org/10.1016/j.matdes.2019.108288

21. Liu D, Wu D, Wang R, et al (2022) Formation mechanism of Al-Zn-Mg-Cu alloy fabricated by laser-arc hybrid additive manufacturing: Microstructure evaluation and mechanical properties. Addit Manuf 50:102554. https://doi.org/10.1016/j.addma.2021.102554

22. Bai JY, Yang CL, Lin SB, et al (2016) Mechanical properties of 2219-Al components produced by additive manufacturing with TIG. Int J Adv Manuf Technol 86:479–485. https://doi.org/10.1007/s00170-015-8168-x

23. Qi Z, Cong B, Qi B, et al (2018) Microstructure and mechanical properties of double-wire + arc additively manufactured Al-Cu-Mg alloys. J Mater Process Technol 255:347–353. https://doi.org/10.1016/j.jmatprotec.2017.12.019

24. Ram GDJ, Murugesan R, Sundaresan S Fusion zone grain refinement in aluminum alloy welds through magnetic arc oscillation and its effect on tensile behavior

25. Nourollahi A, Shoja Razavi R, Barekat M, et al (2021) Microstructural investigation of direct laser deposition of the Ti–6Al–4V alloy by different melt pool protection conditions. J Mater Res Technol 13:590–601. https://doi.org/10.1016/j.jmrt.2021.04.087

26. Gao Y, Wu C, Peng K, et al (2021) Towards superior fatigue crack growth resistance of TC4-DT alloy by in-situ rolled wire-arc additive manufacturing. J Mater Res Technol 15:1395–1407. https://doi.org/10.1016/j.jmrt.2021.08.152